Computational Mechanics 31 (2003) 69–77 © Springer-Verlag 2003
DOI 10.1007/s00466-002-0394-z

A cohesive segments method for the simulation of crack growth

J. J. C. Remmers, R. de Borst, A. Needleman

Abstract A numerical method for crack growth is described in which the crack is not regarded as a single discontinuity that propagates continuously. Instead, the crack is represented by a set of overlapping cohesive segments. These cohesive segments are inserted into finite elements as discontinuities in the displacement field by exploiting the partition-of-unity property of shape functions. The cohesive segments can be incorporated at arbitrary locations and orientations and are not tied to any particular mesh direction. The evolution of decohesion of the segments is governed by a cohesive law. The independent specification of bulk and cohesive constitutive relations leads to a characteristic length being introduced into the formulation. The formulation permits both crack nucleation and discontinuous crack growth to be modelled. The implementation is outlined and some numerical examples are presented.

Keywords Crack growth, Fracture, Cohesive zones, Partitions of unity

1 Introduction

In conventional engineering fracture mechanics, crack growth is assumed to occur by the extension of a single dominant crack. However, there are a wide variety of circumstances where the fracture process involves the nucleation and growth of multiple crack-like flaws. For example, in heterogeneous materials, multiple cracks that initiate and grow in one phase may link up by nucleating cracks in another phase or by propagating across phase boundaries, e.g. [1]. Another example is the transition from subsonic to intersonic crack speeds via the nucleation of a micro-crack ahead of the main crack, [2]. Also, in quasi-brittle materials micro-cracking in front of the main crack tip plays a key role in setting the fracture toughness [3]. Hence, a need for analysing discontinuous crack growth arises in a wide variety of contexts.

A cohesive surface methodology has emerged which permits the analysis of fracture processes in which there is no dominant flaw. In fact, an initial crack-like defect is not required since crack nucleation can occur naturally during the loading history. The basic assumption of the cohesive surface framework is that the separation process is confined to a set of discrete planes (or lines in a two-dimensional context). A constitutive relation is then specified for each cohesive surface that allows separation to occur.

The cohesive approach to fracture was pioneered by Barenblatt [4], Dugdale [5] and Hillerborg et al. [6]. In these formulations, a dominant flaw was assumed present as in conventional engineering fracture mechanics, but a cohesive zone was introduced ahead of the existing crack tip. The relation between the work expended in this cohesive zone and that in the crack tip field is typically such that the stress singularity is cancelled and the near tip stresses are finite. The slip weakening model of Andrews [7] introduced in the geophysics literature did not require crack growth to be continuous. The cohesive framework was extended to finite deformations and to situations without an initial crack in [8]. Subsequently, a wide variety of fracture phenomena have been analysed using the cohesive surface methodology.

In a cohesive surface formulation, constitutive relations are specified independently for the bulk material and for one or more cohesive surfaces, see [8, 9]. The cohesive constitutive relation embodies the failure characteristics of the material and characterises the separation process. The bulk and cohesive constitutive relations together with appropriate balance laws and boundary (and initial) conditions completely specify the problem. Fracture, if it takes place, emerges as a natural outcome of the deformation process without introducing any additional failure criterion. The simplest cohesive constitutive relation is one where the cohesive surface traction is a function of the displacement jump across the cohesive surface. Such a cohesive constitutive relation incorporates as parameters the strength f_t and the work of separation (or fracture energy) $\mathcal{G}_c$. From dimensional considerations, this introduces a characteristic length.

J. J. C. Remmers (✉), R. de Borst
Faculty of Aerospace Engineering, Koiter Institute Delft,
Delft University of Technology, PO Box 5058,
2600 GB, Delft, The Netherlands
e-mail: J.J.C.Remmers@LR.TUDelft.nl

A. Needleman
Division of Engineering, Brown University,
Providence, Rhode Island 02912, USA

Dedicated to the memory of Prof. Mike Crisfield, for his cheerfulness and cooperation as a colleague and friend over many years.

The authors wish to express their thanks to Erik-Jan Lingen for his help in the implementation of the model in the JIVE finite element toolbox. AN is grateful for support from the Office of Naval Research through grant N00014-97-1-0179.

When fracture takes place along well-defined interfaces as, for example, in a lamellar solid, the placement of cohesive surfaces is clear. Also when the crack path is known in advance from experiments, accurate predictions can be obtained, since interface elements can be placed along the known crack path [10]. However, for a solid that is homogeneous on the scale modelled, the placement of cohesive surfaces is problematic. In Xu and Needleman [9] multiple cohesive surfaces were used and in their calculations cohesive interface elements were placed along all finite element mesh boundaries. Although this approach simplifies the simulation of complex crack phenomena such as crack branching and crack initiation away from a main crack tip, it is not mesh independent. In fact, since the interface elements are aligned with the element boundaries, the orientation of cracks is restricted to a limited number of predefined angles. In addition, if, as in [9], the cohesive surfaces are taken to have a nonzero initial compliance, the presence of the cohesive surfaces contributes to the overall compliance of the body. Then, if cohesive surfaces are added between all elements as the computational mesh is refined, the overall compliance depends on the mesh and an ill-posed problem results. A well-posed problem is obtained if a mesh-independent cohesive surface spacing is used, but it is unclear how to set that spacing for homogeneous solids. To overcome limitations associated with initially compliant cohesive surfaces, Camacho and Ortiz [11] used initially rigid cohesive surfaces in conjunction with adaptive mesh refinement. The use of initially rigid cohesive surfaces introduces other difficulties, at least in modelling dynamic crack growth [12, 13].

For a certain class of problems, an alternative is to adopt a smeared crack approach, in which the separation energy $\mathcal{G}_c$ is distributed over the element width, e.g. [10, 14–16]. Finite element methods with embedded discontinuities provide a means of implementing smeared cohesive models [17, 18]. The embedded discontinuity approaches enhance the deformational capabilities of the elements, especially when the standard Bubnov-Galerkin approach is replaced by a Petrov-Galerkin method, which properly incorporates the discontinuity kinematics [19]. The high local strain gradients inside localisation bands are captured more accurately at the expense of obtaining a nonsymmetric stiffness matrix. However, a true discontinuity is not obtained because the kinematics of the embedded localisation band are diffused over the element when the governing equations are cast in a weak format, either via a Bubnov-Galerkin or via a Petrov-Galerkin procedure. Several authors [20, 21] have proved the equivalence between embedded discontinuity approaches and classical smeared-crack models in which the separation energy is smeared out over the element width. Accordingly, the embedded discontinuity approaches inherit many of the disadvantages of conventional smeared-crack models, including the sensitivity of crack propagation to the direction of the mesh lines.

There are advantages to incorporating the cohesive surfaces (or zones) into continuum finite elements by using the partition-of-unity property of finite element shape functions [22] in conjunction with a discontinuous mode incorporated at the element level [23]. The cohesive zone is then modelled as a jump in the displacement field of the continuum element [20, 24–27]. The magnitude of the displacement jump is determined by additional degrees of freedom which are added at the existing nodes. A key feature of the method is the possibility of extending the cohesive crack during the calculation in an arbitrary direction, independent of the structure of the underlying finite element mesh. When cohesive surfaces are added during the calculation, there is no need for a high initial stiffness to minimise the effect of increasing the initial compliance of the medium due to the presence of cohesive surface elements. As a consequence, numerical anomalies, such as stress oscillations at the interface [28] or spurious stress wave reflections are avoided, but other anomalies may be introduced in dynamic problems [12, 13].

A drawback of the current version of partition-of-unity based cohesive zone numerical methods is that the crack is regarded as a single entity. Crack propagation is modelled by extending the current displacement jump. Thus, continuous growth of a crack as in the original cohesive zone formulations of Barenblatt [4], Dugdale [5] and Hillerborg et al. [6] can be modelled, but not discontinuous crack growth involving crack initiation at multiple locations and the subsequent growth and coalescence of the nucleated cracks.

Here, we develop a cohesive finite element method based on incorporating segments of cohesive surfaces into continuum finite elements that is applicable when crack growth is discontinuous. The crack is not regarded as a single entity. Instead, it is modelled as a collection of overlapping cohesive segments, which are added as displacement jumps by using the partition-of-unity property of finite element shape functions. A combination of overlapping crack segments can behave as a continuous crack. In addition, since crack segments can be added at arbitrary positions and with arbitrary orientations, the method allows for complex crack patterns including the simulation of crack nucleation at multiple locations, followed by growth and coalescence. Branching of an existing crack is also allowed for.

We begin with a short description of the approach. Then, the underlying kinematic relations for a domain with multiple displacement jumps is discussed with attention restricted to a small deformation formulation. Next, some details regarding the implementation are given. The paper concludes with some numerical examples.

2
Cohesive segments model

The physics of crack initiation and crack growth in a heterogeneous quasi-brittle material is illustrated in Fig. 1 [1] which shows a concrete specimen loaded in tension. The heterogeneity of the material, i.e. the presence of particles of different sizes and stiffnesses, leads to a complex stress field in which new cracks nucleate ("a" in Fig. 1) and existing cracks branch ("b" in Fig. 1). Smeared (cohesive-zone) models are not able to capture these processes of crack initiation, growth, coalescence and branching properly, since essential characteristics are lost in the averaging process.

The cohesive segments approach can, at least in principle, describe the physical processes observed in Fig. 1.

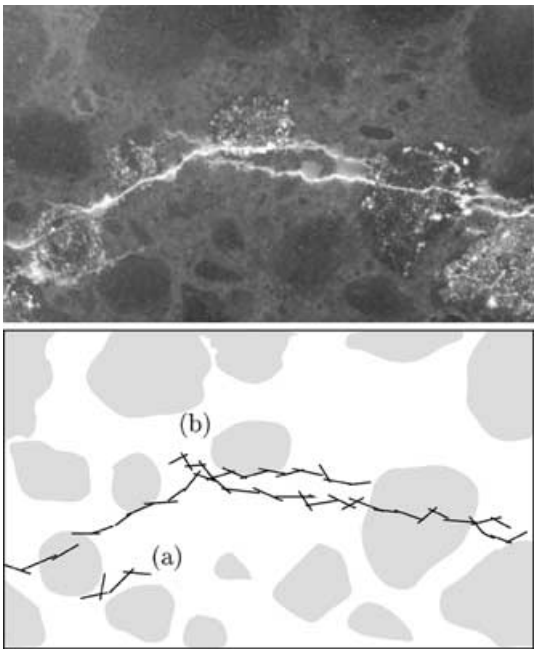

Fig. 1. Experimentally observed 'diffuse' crack pattern [1] and possible representation with cohesive segments

Although a wide variety of cohesive constitutive relations can be incorporated into the cohesive segments framework, in the computations here no cohesive segments are present at the beginning of a calculation which means that an initially rigid cohesive constitutive relation is assumed. When decohesion initiates, a cohesive segment is inserted through the integration point. The segment is taken to extend throughout the element to which the integration point belongs and into the neighbouring elements, see Fig. 3. The evolution of the crack segment is governed by a decohesion constitutive relation. Thus, we need to specify: (i) a criterion for the initiation of decohesion; (ii) a criterion for the orientation of the added cohesive segment; and (iii) the decohesion constitutive relation.

In the illustrative examples here only normal (mode-I) decohesion is considered. The initiation of decohesion is taken to occur when the maximum principal stress at a finite element integration point exceeds the cohesive strength f_t. The orientation of the cohesive surface is specified as being normal to the maximum principal stress direction. The decohesion constitutive relation is taken to have the exponential form,

$$t_n = f_t \exp\left(-\frac{f_t}{\mathcal{G}_c}\kappa\right), \tag{1}$$

where t_n is the normal traction across the cohesive surface, $\mathcal{G}_c$ is the work of separation and κ, which has dimensions of reciprocal length, is a specified cohesive parameter. Since only mode-I separation is considered, the shear traction across the cohesive surface vanishes. The cohesive segments are inserted into existing finite elements by exploiting the partition-of-unity property of their shape functions, thus ensuring that the discrete character of the cohesive segment is preserved in the discretisation process. Note that the orientation of the cohesive segments is not tied to any direction associated with the discretisation.

3
Kinematic relations

The key feature of the cohesive segments approach is the possible emergence of multiple cracks in a domain. Consider the domain Ω with boundary Γ as shown in Fig. 2. It contains m discontinuities $\Gamma_{d,j}$, where $j = 1, m$. Each discontinuity splits the domain in two parts, which are denoted as Ω_j^- and Ω_j^+. For all discontinuities the following relation must hold:

$$\Omega_j^- \cup \Omega_j^+ = \Omega \quad \forall j = 1, m \ . \tag{2}$$

The displacement field in the domain Ω consists of a continuous regular displacement field $\hat{\mathbf{u}}$ plus m additional continuous displacement fields $\tilde{\mathbf{u}}_j$, cf. [29]:

$$\mathbf{u}(\mathbf{x}, t) = \hat{\mathbf{u}}(\mathbf{x}, t) + \sum_{j=1}^{m} \mathcal{H}_{\Gamma_{d,j}}(\mathbf{x})\tilde{\mathbf{u}}_j(\mathbf{x}, t) \ , \tag{3}$$

where $\mathbf{x}$ denotes the position of a material point, t is time and $\mathcal{H}_{\Gamma_{d,j}}$ are Heaviside step functions, defined as:

$$\mathcal{H}_{\Gamma_{d,j}}(\mathbf{x}) = \begin{cases} 0 & \text{if } \mathbf{x} \in \Omega_j^-, \\ 1 & \text{if } \mathbf{x} \in \Omega_j^+ \ . \end{cases} \tag{4}$$

The strain field in the bulk can be found by taking the derivative of the displacement field, Eq. (3):

$$\epsilon(\mathbf{x}, t) = \nabla^s \hat{\mathbf{u}}(\mathbf{x}, t) + \sum_{j=1}^{m} \mathcal{H}_{\Gamma_{d,j}}(\mathbf{x})\nabla^s \tilde{\mathbf{u}}_j(\mathbf{x}, t) \ , \tag{5}$$

where a superscript s denotes the symmetric part of a differential operator. Note that at the discontinuities $\Gamma_{d,j}$, the strains are not defined. There, the magnitude of the displacement jump

$$\mathbf{v}_j(\mathbf{x}, t) = \tilde{\mathbf{u}}_j(\mathbf{x}, t) \quad \mathbf{x} \text{ on } \Gamma_{d,j} \ , \tag{6}$$

is the relevant kinematic quantity. Although the formulation can be applied to finite deformations [25, 26], we restrict attention to small displacement gradients.

4
Equilibrium equations

Consider the quasi-static equilibrium equations without body forces and the corresponding boundary conditions:

$$\nabla \cdot \boldsymbol{\sigma} = \mathbf{0} \quad \mathbf{x} \in \Omega \ , \tag{7}$$

$$\mathbf{n}_t \cdot \boldsymbol{\sigma} = \bar{\mathbf{t}} \quad \mathbf{x} \in \Gamma_t \ , \tag{8}$$

$$\mathbf{u} = \bar{\mathbf{u}} \quad \mathbf{x} \in \Gamma_u \ , \tag{9}$$

$$\mathbf{n}_{d,j} \cdot \boldsymbol{\sigma} = \mathbf{t}_j \quad \mathbf{x} \in \Gamma_{d,j} \ , \tag{10}$$

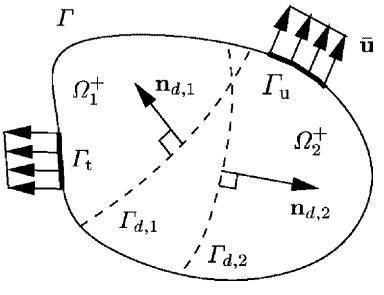

Fig. 2. Domain Ω crossed by two discontinuities, $\Gamma_{d,1}$ and $\Gamma_{d,2}$ (dashed lines)

where $\boldsymbol{\sigma}$ is the Cauchy stress in the bulk material, $\bar{\mathbf{t}}$ are the prescribed tractions on Γ_t with outward normal vector $\mathbf{n}_t$, $\bar{\mathbf{u}}$ are the prescribed displacements on Γ_u and $\mathbf{t}_j$ are the tractions at discontinuity $\Gamma_{d,j}$. The normal $\mathbf{n}_{d,j}$ points from Ω_j^- to Ω_j^+. Equilibrium can be expressed in a weak form by multiplication with an admissible variational displacement field $\boldsymbol{\eta}$:

$$\int_\Omega \boldsymbol{\eta} \cdot (\nabla \cdot \boldsymbol{\sigma}) \mathrm{d}\Omega = 0 \ . \tag{11}$$

Taking the space of the admissible variations to be the same as the actual displacement field, Eq. (3), the variations of the displacements can be decomposed as:

$$\boldsymbol{\eta} = \hat{\boldsymbol{\eta}} + \sum_{j=1}^{m} \mathcal{H}_{\Gamma_{d,j}} \tilde{\boldsymbol{\eta}}_j \ . \tag{12}$$

Substituting the variations into Eq. (11) gives:

$$\int_\Omega \hat{\boldsymbol{\eta}} \cdot (\nabla \cdot \boldsymbol{\sigma}) \mathrm{d}\Omega + \sum_{j=1}^{m} \int_\Omega \mathcal{H}_{\Gamma_{d,j}} \tilde{\boldsymbol{\eta}}_j \cdot (\nabla \cdot \boldsymbol{\sigma}) \mathrm{d}\Omega = 0 \ . \tag{13}$$

We now apply Gauss' theorem, use the symmetry of the Cauchy stress tensor, eliminate the Heaviside functions in the bulk by changing the integration domain and use the boundary conditions at the external boundary Γ_t and at the discontinuity planes $\Gamma_{d,j}$ to give:

$$\begin{aligned} &\int_\Omega \nabla^s \hat{\boldsymbol{\eta}} : \boldsymbol{\sigma} \, \mathrm{d}\Omega + \sum_{j=1}^{m} \int_{\Omega_j^+} \nabla^s \tilde{\boldsymbol{\eta}}_j : \boldsymbol{\sigma} \, \mathrm{d}\Omega + \sum_{j=1}^{m} \int_{\Gamma_{d,j}} \tilde{\boldsymbol{\eta}}_j \cdot \mathbf{t}_j \, \mathrm{d}\Gamma \\ &\quad = \int_{\Gamma_t} \hat{\boldsymbol{\eta}} \cdot \bar{\mathbf{t}} \, \mathrm{d}\Gamma + \sum_{j=1}^{m} \int_{\Gamma_t} \mathcal{H}_{\Gamma_{d,j}} \, \tilde{\boldsymbol{\eta}}_j \cdot \bar{\mathbf{t}} \, \mathrm{d}\Gamma \ . \end{aligned} \tag{14}$$

5 Finite element formulation

For the finite element formulation, we use the partition-of-unity property of finite element shape functions [22]. A collection of functions ϕ_i, associated with node i $(1 \leq i \leq n)$ form a partition of unity if:

$$\sum_{i=1}^{n} \phi_i = 1 \ . \tag{15}$$

For any set of functions that satisfy this equation, a field u can be interpolated as follows:

$$u(\mathbf{x}, t) = \sum_{i=1}^{n} \phi_i(\mathbf{x}) \left(a_i(t) + \sum_{j=1}^{m} \beta_j(\mathbf{x}) b_{ij}(t) \right) \ , \tag{16}$$

with $a_i(t)$ the regular nodal degrees-of-freedom, $\beta_j(\mathbf{x})$ the enhanced basis terms and b_{ij} the additional degrees of freedom at node i, representing the amplitude of the jth basis term β_j. The displacement fields $\mathcal{H}_{\Gamma_{d,j}} \tilde{\mathbf{u}}_j$ can be considered as enhanced basis fields. By replacing $\beta_j(\mathbf{x})$ by the corresponding Heaviside function $\mathcal{H}_{\Gamma_{d,j}}$, we can cast the displacement field in Eq. (3) in the following discrete form:

$$\mathbf{u} = \mathbf{N}\mathbf{a} + \sum_{j=1}^{m} \mathcal{H}_{\Gamma_{d,j}} \mathbf{N}\mathbf{b}_j \ , \tag{17}$$

where the vector $\mathbf{a}$ contains the regular nodal degrees of freedom of the element and $\mathbf{b}_j$ contains all additional nodal degrees of freedom associated with discontinuity $\Gamma_{d,j}$. The matrix $\mathbf{N}$ contains the conventional element shape functions. The discretised strain field can be derived by straightforward differentiation:

$$\boldsymbol{\epsilon} = \mathbf{B}\mathbf{a} + \sum_{j=1}^{m} \mathcal{H}_{\Gamma_{d,j}} \mathbf{B}\mathbf{b}_j \ , \tag{18}$$

where $\mathbf{B} = \mathbf{L}\mathbf{N}$ contains the spatial derivatives of the element shape functions. $\mathbf{L}$ is a differential operator matrix, which, for two-dimensional elements, is:

$$\mathbf{L} = \begin{bmatrix} \frac{\partial}{\partial x} & 0 \\ 0 & \frac{\partial}{\partial y} \\ \frac{\partial}{\partial y} & \frac{\partial}{\partial x} \end{bmatrix} \ . \tag{19}$$

Finally, the discrete displacement jump at discontinuity $\Gamma_{d,j}$, see Eq. (6), is equal to:

$$\mathbf{v}_j = \mathbf{N}\mathbf{b}_j \ . \tag{20}$$

In the spirit of a Bubnov-Galerkin approach, the variations of the displacement fields can be discretised as:

$$\begin{aligned} &\hat{\boldsymbol{\eta}} = \mathbf{N}\delta\mathbf{a} \qquad \tilde{\boldsymbol{\eta}}_j = \mathbf{N}\delta\mathbf{b}_j \\ &\nabla^s\hat{\boldsymbol{\eta}} = \mathbf{B}\delta\mathbf{a} \quad \nabla^s\tilde{\boldsymbol{\eta}}_j = \mathbf{B}\delta\mathbf{b}_j \ . \end{aligned} \tag{21}$$

Inserting them into the weak form of the equilibrium equation (10) yields:

$$\begin{aligned} &\int_\Omega (\mathbf{B}\delta\mathbf{a})^{\mathrm{T}} \boldsymbol{\sigma} \, \mathrm{d}\Omega + \sum_{j=1}^{m} \int_{\Omega_j^+} (\mathbf{B}\delta\mathbf{b}_j)^{\mathrm{T}} \boldsymbol{\sigma} \, \mathrm{d}\Omega + \sum_{j=1}^{m} \int_{\Gamma_{d,j}} (\mathbf{N}\delta\mathbf{b}_j)^{\mathrm{T}} \mathbf{t}_j \, \mathrm{d}\Gamma \\ &\quad = \int_{\Gamma_t} (\mathbf{N}\delta\mathbf{a})^{\mathrm{T}} \bar{\mathbf{t}} \, \mathrm{d}\Gamma + \sum_{j=1}^{m} \int_{\Gamma_t} \mathcal{H}_{\Gamma_{d,j}} \, (\mathbf{N}\delta\mathbf{b}_j)^{\mathrm{T}} \bar{\mathbf{t}} \, \mathrm{d}\Gamma \ . \end{aligned} \tag{22}$$

By taking all the variations $\delta\mathbf{a}$ and $\delta\mathbf{b}_j$ respectively, the weak equilibrium equations can be separated in a set of $m+1$ equilibrium equations:

$$\begin{aligned} &\int_\Omega \mathbf{B}^{\mathrm{T}} \boldsymbol{\sigma} \, \mathrm{d}\Omega = \int_{\Gamma_t} \mathbf{N}^{\mathrm{T}} \bar{\mathbf{t}} \, \mathrm{d}\Gamma \ , \\ &\int_{\Omega_1^+} \mathbf{B}^{\mathrm{T}} \boldsymbol{\sigma} \, \mathrm{d}\Omega + \int_{\Gamma_{d,1}} \mathbf{N}^{\mathrm{T}} \mathbf{t}_1 \mathrm{d}\Gamma = \int_{\Gamma_t} \mathcal{H}_{\Gamma_{d,1}} \mathbf{N}^{\mathrm{T}} \bar{\mathbf{t}} \, \mathrm{d}\Gamma \ , \\ &\int_{\Omega_2^+} \mathbf{B}^{\mathrm{T}} \boldsymbol{\sigma} \, \mathrm{d}\Omega + \int_{\Gamma_{d,2}} \mathbf{N}^{\mathrm{T}} \mathbf{t}_2 \, \mathrm{d}\Gamma = \int_{\Gamma_t} \mathcal{H}_{\Gamma_{d,2}} \mathbf{N}^{\mathrm{T}} \bar{\mathbf{t}} \, \mathrm{d}\Gamma \ , \\ &\qquad \vdots \\ &\int_{\Omega_m^+} \mathbf{B}^{\mathrm{T}} \boldsymbol{\sigma} \, \mathrm{d}\Omega + \int_{\Gamma_{d,m}} \mathbf{N}^{\mathrm{T}} \mathbf{t}_m \, \mathrm{d}\Gamma = \int_{\Gamma_t} \mathcal{H}_{\Gamma_{d,m}} \mathbf{N}^{\mathrm{T}} \bar{\mathbf{t}} \, \mathrm{d}\Gamma \ . \end{aligned} \tag{23}$$

The equilibrium equation that is related to the regular degrees of freedom is identical to the equilibrium equation for an element without a discontinuity. Therefore, it is possible

to add a discontinuity to an element during the calculations with a minimal effort by adding the additional equilibrium relations and the corresponding degrees of freedom $\mathbf{b}_j$.

5.1 Constitutive relations

The stress rate in the bulk material $\dot{\boldsymbol{\sigma}}$ is a function of the strain rate $\dot{\boldsymbol{\epsilon}}$ and can be written as, see also Eq. (18):

$$\dot{\boldsymbol{\sigma}} = \mathbf{D}\dot{\boldsymbol{\epsilon}} = \mathbf{D}\left(\mathbf{B}\dot{\mathbf{a}} + \sum_{j=1}^{m} \mathcal{H}_{\Gamma_{d,j}} \mathbf{B}\dot{\mathbf{b}}_j\right) \quad , \tag{24}$$

where $\dot{(\,)}$ denotes $\partial(\,)/\partial t$ and $\mathbf{D}$ is the tangent stiffness matrix of the bulk material (rate independent material behaviour is assumed here). The traction rates $\dot{\mathbf{t}}_j$ at the jth discontinuity can be expressed in terms of the corresponding enhanced nodal velocities $\dot{\mathbf{v}}_j$, Eq. (20):

$$\dot{\mathbf{t}}_j = \mathbf{T}\dot{\mathbf{v}}_j = \mathbf{T}\mathbf{N}\dot{\mathbf{b}}_j \quad , \tag{25}$$

where $\mathbf{T}$ is the tangent stiffness of the traction-separation law at the discontinuity. The latter relations are defined in a local frame of reference, aligned with the discontinuity. Therefore, they must be transformed into the element local frame of reference.

5.2 Linearisation of the equilibrium equations

The deformation history is calculated in an incremental fashion. At each time step the rate equilibrium equations are differentiated with respect to the displacement variables $\mathbf{a}$ and $\mathbf{b}_j$. Differentiating the rate form of the discretised equilibrium equations (23) leads to

$$\begin{bmatrix} \mathbf{K}_{aa} & \mathbf{K}_{ab_1} & \dots & \mathbf{K}_{ab_m} \\ \mathbf{K}_{ab_1} & \mathbf{K}_{b_1b_1} & \dots & \mathbf{K}_{b_1b_m} \\ \vdots & \vdots & \ddots & \vdots \\ \mathbf{K}_{ab_m} & \mathbf{K}_{b_1b_m} & \dots & \mathbf{K}_{b_mb_m} \end{bmatrix} \begin{bmatrix} \dot{\mathbf{a}} \\ \dot{\mathbf{b}}_1 \\ \vdots \\ \dot{\mathbf{b}}_m \end{bmatrix} = \begin{bmatrix} \mathbf{f}_a^{\text{ext}} \\ \mathbf{f}_{b_1}^{\text{ext}} \\ \vdots \\ \mathbf{f}_{b_m}^{\text{ext}} \end{bmatrix} - \begin{bmatrix} \mathbf{f}_a^{\text{int}} \\ \mathbf{f}_{b_1}^{\text{int}} \\ \vdots \\ \mathbf{f}_{b_m}^{\text{int}} \end{bmatrix} \quad , \tag{26}$$

where the terms in the stiffness matrix are:

$$\begin{aligned} \mathbf{K}_{aa} &= \int_{\Omega} \mathbf{B}^{\mathrm{T}}\mathbf{D}\mathbf{B}\,\mathrm{d}\Omega \quad , \\ \mathbf{K}_{ab_j} &= \int_{\Omega_j^+} \mathbf{B}^{\mathrm{T}}\mathbf{D}\mathbf{B}\,\mathrm{d}\Omega \quad , \\ \mathbf{K}_{b_jb_j} &= \int_{\Omega_j^+} \mathbf{B}^{\mathrm{T}}\mathbf{D}\mathbf{B}\,\mathrm{d}\Omega + \int_{\Gamma_{d,j}} \mathbf{N}^{\mathrm{T}}\mathbf{T}\mathbf{N}\,\mathrm{d}\Gamma \quad , \\ \mathbf{K}_{b_jb_k} &= \int_{\Omega_j^+ \cap \Omega_k^+} \mathbf{B}^{\mathrm{T}}\mathbf{D}\mathbf{B}\,\mathrm{d}\Omega \qquad \text{if } j \neq k \quad . \end{aligned} \tag{27}$$

The internal forces are given by:

$$\begin{aligned} \mathbf{f}_a^{\text{int}} &= \int_{\Omega} \mathbf{B}^{\mathrm{T}}\boldsymbol{\sigma}\,\mathrm{d}\Omega \quad , \\ \mathbf{f}_{b_j}^{\text{int}} &= \int_{\Omega_j^+} \mathbf{B}^{\mathrm{T}}\boldsymbol{\sigma}\,\mathrm{d}\Omega + \int_{\Gamma_{d,j}} \mathbf{N}^{\mathrm{T}}\mathbf{t}_j\,\mathrm{d}\Gamma \quad . \end{aligned} \tag{28}$$

Finally, the expression for the external forces is:

$$\begin{aligned} \mathbf{f}_a^{\text{ext}} &= \int_{\Gamma_t} \mathbf{N}^{\mathrm{T}}\bar{\mathbf{t}}\,\mathrm{d}\Gamma \quad , \\ \mathbf{f}_{b_j}^{\text{ext}} &= \int_{\Gamma_t} \mathcal{H}_{\Gamma_{d,j}}\mathbf{N}^{\mathrm{T}}\bar{\mathbf{t}}\,\mathrm{d}\Gamma \quad . \end{aligned} \tag{29}$$

Note that if the tangent matrices $\mathbf{D}$ and $\mathbf{T}$ are symmetric, symmetry of the submatrices $\mathbf{K}_{aa}$, $\mathbf{K}_{ab_j}$ and $\mathbf{K}_{b_jb_k}$ is preserved. Consequently, the total stiffness matrix also remains symmetric.

6 Implementation

The procedure has been implemented using a four-node quadrilateral continuum finite element. A new cohesive segment is added when the major principal stress at an integration point within an element reaches the cohesive strength f_t in Eq. (1). The added cohesive segment passes through the integration point and extends through the entire element and into the neighbouring elements to the boundary of a patch of elements influenced by the added degrees of freedom, see Fig. 3. Various criteria can be used to determine the direction of the cohesive segment, but here the cohesive segment is taken to be normal to the major principal stress direction at the integration point.

Since the cohesive segment is taken to be a straight line, the normal vector $\mathbf{n}_{d,j}$ is constant along the patch of elements. The magnitude of the displacement jump of the segment is governed by a set of additional degrees of freedom, which are added to all four nodes of the central

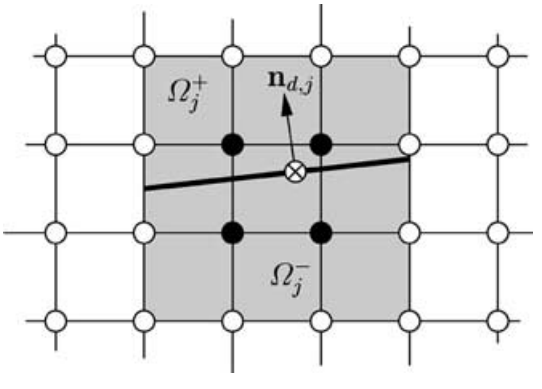

Fig. 3. A single cohesive segment in a quadrilateral mesh. The segment passes through an integration point (⊗) where the cohesive strength is attained. The dark nodes contain additional degrees of freedom $\mathbf{b}_j$ that determine the magnitude of the displacement jump. The gray shade denotes the elements that belong to the patch that is influenced by the cohesive segment

element of the patch. Since the nodes at the edge of the patch do not contain additional degrees of freedom, the displacement jump at the edge vanishes, thus ensuring a zero opening at the tip of the cohesive segment [24].

Since the additional degrees of freedom cannot be condensed at an element level, they influence all the surrounding elements in the patch (denoted by the gray shade). For the elements that belong to the patch, but do not contain a cohesive segment, the additional displacement $\tilde{\mathbf{u}}_j$ is not premultiplied with a Heaviside function, but with a value, which is zero when the element belongs to the Ω_j^- part of the domain, and equals one when the element is in the Ω_j^+ part.

A key feature of the approach is the possibility of having overlapping cohesive segments. In the situation sketched in Fig. 4, a new cohesive segment is added next to an existing segment. The displacement jump of the new cohesive segment is supported by an additional set of degrees of freedom, and is added to the nodes of the central element of the new segment (denoted by black squares). This new set has no relation to the additional degrees of freedom of the first segment. The hatched elements are elements in the patches that belong to both segments. In these elements two additional sets of degrees of freedom are present, although each set of degrees of freedom is added to a different set of nodes.

Another possible configuration is shown in Fig. 5 where two segments cross to form a cohesive zone with a sharp bend. Here, the patches overlap in such a way that one node contains additional sets of degrees of freedom associated with both segments. Again, this configuration will act as a single cohesive zone on a global level.

Numerical integration of an element that contains one or more discontinuities is not trivial. Since the displacement fields are only piecewise continuous, standard integration techniques are no longer accurate. One alternative is to divide the element into subdomains, see Fig. 6. Since the displacement field is continuous within each subdomain, the integrals over the subdomain can be evaluated numerically with standard integration techniques. A second possibility is to integrate such an element using a large number of fixed integration points. A possible candidate is Simpson's rule. Although the error with this integration scheme is greater than that associated with the first alternative the effect on the global accuracy of the computation will generally be small, since these elements are usually nearly stress free.

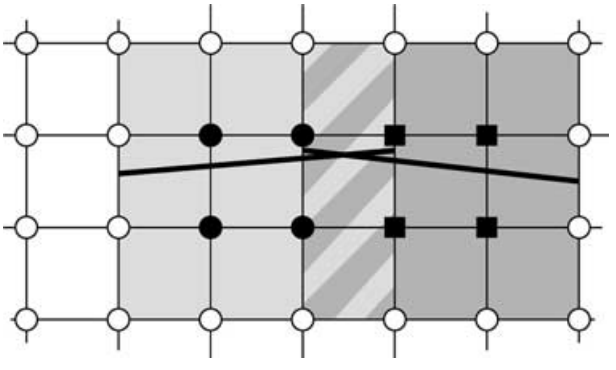

Fig. 4. Interaction of two cohesive segments. The hatched elements have two sets of additional degrees of freedom. The dark circles denote the nodes that contain the additional degrees of freedom for the segment on the left and the dark squares denotes those on the right

7
Numerical examples

Some features of the cohesive segments method are illustrated in a few simple problems. The material behaviour is taken to be described by isotropic elasticity and only mode-I (tensile) separation is considered. However, the cohesive surfaces formulation places no restriction on the material constitutive relation and allows for mixed mode crack growth. A double-cantilever beam with an initial notch with length 1 mm as shown in Fig. 7 [30] is considered. The beam is loaded by peel forces P. The two layers of the beam have identical elastic properties: Young's modulus $E = 100$ N/mm^2 and Poisson's ratio $\nu = 0.3$. The tensile strength of the adhesive is $f_t = 1.0$ N/mm^2 and the work of separation is $\mathcal{G}_c = 0.1$ N/mm. It is

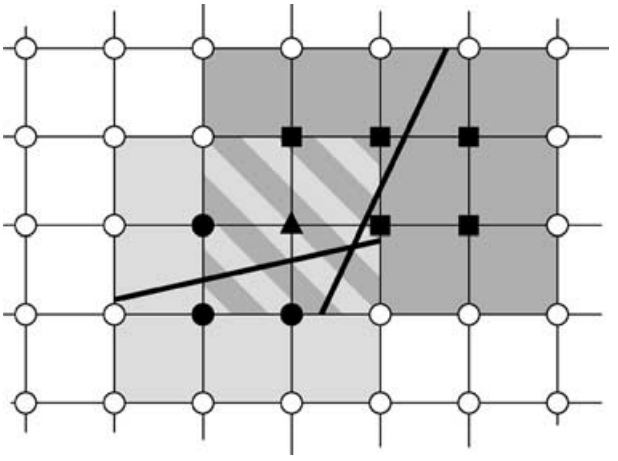

Fig. 5. Crossing of two cohesive segments. The lighter shade of gray denotes the patch of elements to the left hand cohesive segment. The dark circles the nodes that contains the enhanced degrees of freedom. The darker shade of gray and the black squares denote the elements and the nodes that belong to the right-hand segment. The dark triangle denotes the node that contains additional degrees of freedom of both segments

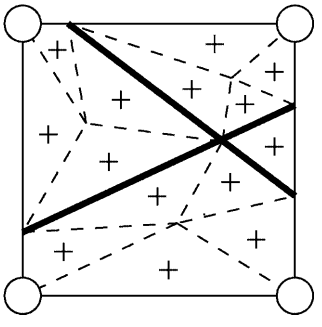

Fig. 6. Numerical integration of an element with two discontinuities (heavy lines). The subdomains (denoted with dashed lines) are integrated with a Gauss scheme with one integration point (+) each

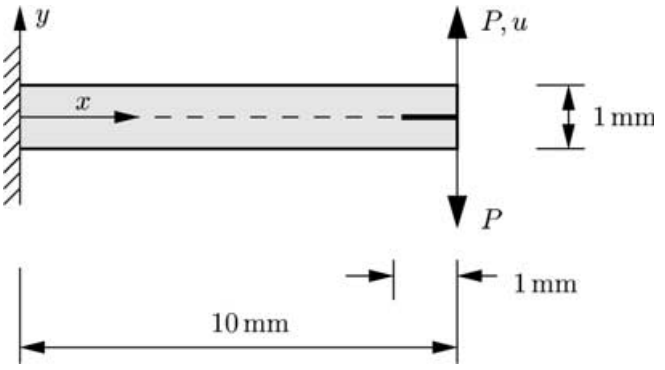

Fig. 7. Double-cantilever beam with an initial notch subjected to peel forces P

assumed that the fracture mode is purely mode-I, the shear traction is identically zero and the decohesion relation is given by Eq. (1), which can be differentiated to give the material tangent matrix:

$$\mathbf{T} = \begin{bmatrix} -\frac{f_t^2}{\mathcal{G}_c}\exp\left(-\frac{f_t}{\mathcal{G}_c}\kappa\right) & 0 \\ 0 & 0 \end{bmatrix}. \tag{30}$$

The specimen is analysed with a mesh having 200×7 elements. The initial notch is modelled as a series of overlapping traction-free cohesive segments which are added to the mesh beforehand.

Since the adhesive is relatively weak, the crack growth trajectory is known, i.e. the interface between the two beams. Therefore, we have only monitored the normal stresses in the y-direction at the interface as the new segment is always aligned with the x-axis. The results are shown in Fig. 8 which gives the load–displacement curve and in Fig. 9 which gives the deformed specimen at the final load step, when $u = 6$ mm. The cohesive segments approach gives results that are nearly identical to those obtained with a method in [30] where a continuous crack is modelled using the partition-of-unity property of finite element shape functions. The areas below the curve, which are a measure of the energy dissipation, are virtually the same for the two calculations. It is noted that there is a high stress concentration in a relatively small area around

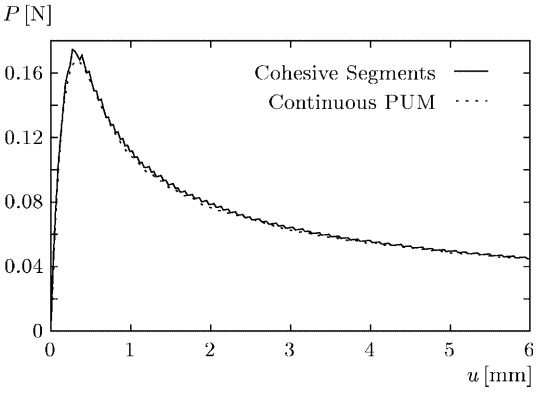

Fig. 8. Load–displacement curve of double-cantilever beam as calculated using the cohesive segments method and a continuous partition of unity method (PUM) [30]

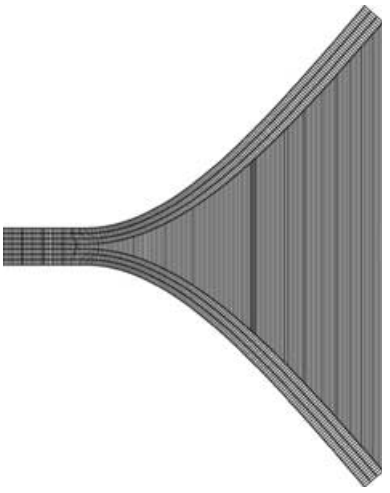

Fig. 9. Final deformation of double-cantilever beam. Note that the deformations are not magnified

the crack tip in this example. To capture the high peak stresses accurately, a rather fine mesh is needed.

In order to demonstrate the ability to simulate discontinuous crack growth, the previous example is slightly modified. A double-cantilever beam is now considered that is identical to the one in Fig. 7 except for a small cavity with length 0.25 mm and height 0.14 mm at a distance 2 mm from the loaded edge, see Fig. 10. During loading, the crack at the initial notch propagates into the cavity. Upon further loading, a new crack nucleates at the opposite side of the cavity and continues along the weak interface. This transition is indicated by the steep jump in the load–displacement curve in Fig. 11. The position of cohesive segments immediately after the nucleation of the second crack, position (A) in the load-displacement curve, is shown in Fig. 12.

The third example illustrates crack nucleation without any initial crack. The specimen is now clamped at both sides and has no initial crack, see Fig. 13. The structure is loaded by forces P. In order to preserve symmetry of crack growth, the specimen is modelled with an odd number of elements (199 in the calculation here) in the x direction.

When $P \approx 0.45$ N, a small crack initiates in the centre of the beam. Due to the size of the discrete load steps, this initial crack consists of three overlapping cohesive segments, which nucleate at the same load step. The crack propagates in both directions with the same velocity. The load increases until the external load is 1.2 N, see Fig. 14.

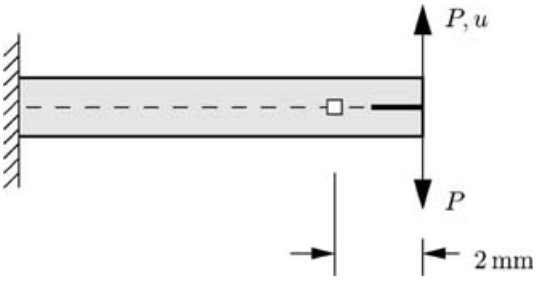

Fig. 10. Geometry of double-cantilever beam with a small cavity

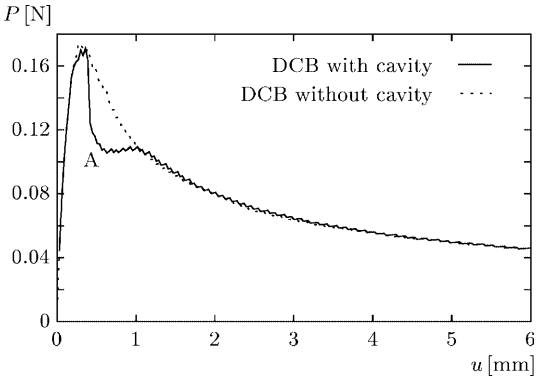

Fig. 11. Load–displacement curve for double-cantilever beam with cavity

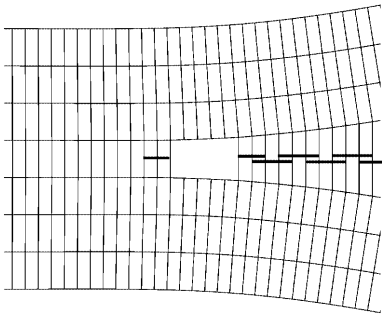

Fig. 12. Position of cohesive segments, denoted by the heavy lines, in the double-cantilever beam with cavity. The individual segments are slightly shifted horizontally for the sake of comprehensibility

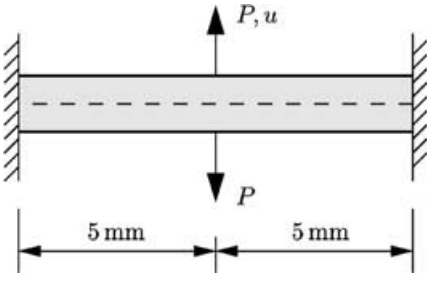

Fig. 13. Double-cantilever beam under central lateral loading

Subsequently, crack growth continues under decreasing load. Figure 15 shows the deformed specimen at the final load step.

8 Concluding remarks

A method for modelling crack growth has been described in which a crack is represented by a collection of cohesive segments with a finite length. The segments are added to finite elements by using the partition-of-unity property of the finite element shape functions. The method permits crack nucleation and discontinuous crack growth to be modelled, irrespective of the structure of the finite element mesh. The numerical formulation is a moderate extension to existing methods which capture discontinuities using

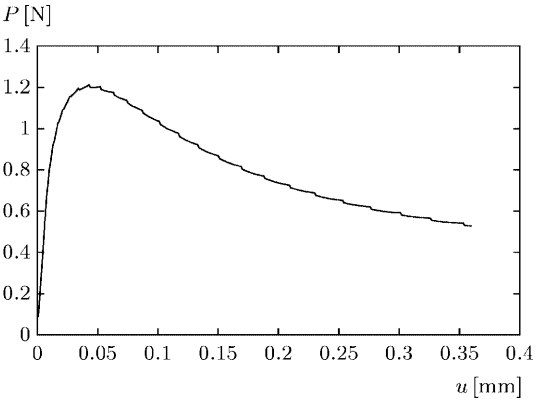

Fig. 14. Load–displacement curve of double-cantilever beam under central lateral loading

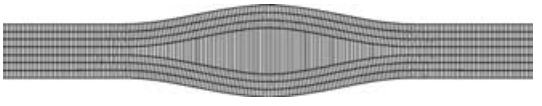

Fig. 15. Deformation of double-cantilever beam under central lateral loading

the partition-of-unity property of finite element shape functions. Nevertheless, the actual implementation of the method can be somewhat elaborate from a bookkeeping point of view, since a single element can be crossed by multiple cracks, each with its own additional degrees of freedom.

Some capabilities of the cohesive segments method have been illustrated by simple two dimensional examples. The extension of the formulation to more complex bulk and cohesive constitutive relations and to three dimensions is straightforward in principle. The ability of the method to capture complex crack patterns accurately, such as shown in Fig. 1, remains to be demonstrated. However, the initial studies here suggest that the cohesive segments method provides a promising approach for modelling complex fracture behaviour.

References

1. **van Mier JGM** (1997) Fracture Processes of Concrete. CRC Press, Boca Raton, Florida
2. **Coker D, Rosakis AJ, Needleman A** (2003) Dynamic crack growth along a polymer composite-homalite interface. J. Mech. Phys. Solids 51: 425–460
3. **Cotterell B, Mai YW** (1996) Fracture Mechanics of Cementitious Materials. Blackie, Glasgow, Scotland
4. **Barenblatt GI** (1962) The mathematical theory of equilibrium cracks in brittle fracture. Adv. Appl. Mech. 7: 55–129
5. **Dugdale DS** (1960) Yielding of steel sheets containing slits. J. Mech. Phys. Solids 8: 100–108
6. **Hillerborg A, Modeer M, Petersson PE** (1976) Analysis of crack formation and crack growth in concrete by means of fracture mechanics and finite elements. Cement Concrete Res. 6: 773–782
7. **Andrews DJ** (1976) Rupture velocity of plane strain shear cracks. J. Geophys. Res. 81: 5679–5687
8. **Needleman A** (1987) A continuum model for void nucleation by inclusion debonding. J. Appl. Mech. 54: 525–531
9. **Xu XP, Needleman A** (1994) Numerical simulations of fast crack growth in brittle solids. J. Mech. Phys. Solids 42: 1397–1434

10. **Rots JG** (1991) Smeared and discrete representations of localized fracture. Int. J. Fract. 51: 45–59
11. **Camacho GT, Ortiz M** (1996) Computational modelling of impact damage in brittle materials. Int. J. Solids Struct. 33: 2899–2938
12. **Falk ML, Needleman A, Rice JR** (2001) A critical evaluation of cohesive zone models of dynamic fracture. Journal de Physique IV 11 Pr5: 43–50
13. **Papoulia KD, Sam CH, Vavasis SA** (2003) Time continuity in cohesive finite element modelling. Int. J. Numer. Meth. Eng. (submitted)
14. **Bažant ZP, Oh B** (1983) Crack band theory for fracture of concrete. RILEM Materials and Structures 16: 155–177
15. **Crisfield MA** (1982) Accelerated solution techniques and concrete cracking. Comput. Meth. Appl. Mech. Eng. 33: 585–607
16. **de Borst R, Nauta P** (1985) Non-orthogonal cracks in a smeared finite element model. Eng. Comput. 2: 35–46
17. **Ortiz M, Leroy Y, Needleman A** (1987) A finite element method for localized failure analysis. Comput. Meth. Appl. Mech. Eng. 61: 189–214
18. **Belytschko T, Fish J, Engelman BE** (1988) A finite element with embedded localization zones. Comput. Meth. Appl. Mech. Eng. 70: 59–89
19. **de Borst R, Wells GN, Sluys LJ** (2001) Some observations on embedded discontinuity models. Eng. Comput. 18: 241–254
20. **Wells GN** (2001) Discontinuous modelling of strain localisation and failure. Dissertation. Delft University of Technology: Delft
21. **Mosler J, Meschke G** (2002) A comparison of embedded discontinuity approaches with fracture energy based smeared crack models. In: Proceedings of the Fifth Congress on Computational Mechanics, WCCM V. Mang HA, Rammerstorfer FG, Eberhardsteiner J (eds). Vienna University of Technology, Vienna, Austria, Paper 81054
22. **Babuska T, Melenk JM** (1997) The partition of unity method. Int. J. Numer. Meth. Eng. 40: 727–758
23. **Moës N, Dolbow J, Belytschko T** (1999) A finite element method for crack growth without remeshing. Int. J. Numer. Meth. Eng. 46: 131–150
24. **Wells GN, Sluys LJ** (2001) A new method for modeling cohesive cracks using finite elements. Int. J. Numer. Meth. Eng. 50: 2667–2682
25. **Belytschko T, Moës N, Usui S, Parimi C** (2001) Arbitrary discontinuities in finite elements. Int. J. Numer. Meth. Eng. 50: 993–1013
26. **Wells GN, de Borst R, Sluys LJ** (2002) A consistent geometrically non-linear approach for delamination. Int. J. Numer. Meth. Eng. 54: 1333–1355
27. **Moës N, Belytschko T** (2002) Extended finite element method for cohesive crack growth. Eng. Fract. Mech. 69: 813–833
28. **Schellekens JCJ, de Borst R** (1992) On the numerical integration of interface elements. Int. J. Numer. Meth. Eng. 36: 43–66
29. **Daux C, Moës N, Dolbow J, Sukumar N, Belytschko T** (2000) Arbitrary branched and intersecting cracks with the extended finite element method. Int. J. Numer. Meth. Eng. 48: 1741–1760
30. **Remmers JJC, Wells GN, de Borst R** (2001) Analysis of delamination growth with discontinuous finite elements. In: Solids, Structures and Coupled Problems (Proceedings of the Second European Conference on Computational Mechanics), Pamin J (ed.). Cracow University of Technology, Cracow, Poland, CD-ROM